INORGANIC CHEMISTRY FRONTIERS

RESEARCH ARTICLE

View Article Online
View Journal | View Issue

Cite this: *Inorg. Chem. Front.*, 2024, **11**, 5336

Temperature-tunable multiple dielectric switch in hybrid rare-earth perovskites regulated by hierarchical guest dynamics, lanthanide contraction and doping†

Hui Xiao,‡[a] Lin-Yong Sheng,‡[a] Shuai Chen,‡[b] Rui-Kang Huang, *[c,d] Cheng-Hui Zeng,[a] Zi-Yi Du, *[a] Chun-Ting He,[a] Wei-Xiong Zhang *[b] and Xiao-Ming Chen[b]

Dielectric switches play an important role in electrical and electronic devices. Here we report a unique class of cage-like hybrid rare-earth perovskites, $(i\text{-PrNHMe}_2)_2[RbLn(NO_3)_6]$ (Ln = La, Ce, Nd or Sm), capable of functioning as temperature-responsive multiple dielectric switches. The strategic incorporation of a conformationally flexible sphere-like guest $(i\text{-PrNHMe}_2)^+$ cation into the cage-like perovskite framework is in favor of the occurrence of hierarchical guest dynamics accompanied by stepwise phase transitions, leading to seldom observed multiple dielectric switching of "Low ↔ High ↔ Low ↔ High" upon heating. Furthermore, the utilizing of lanthanide contraction or rare-earth doping allows for fine tuning of the switching temperature. In addition, multiaxial ferroelasticity is found in these perovskites. Overall, this study provides a good approach for the design of temperature-tunable multiple dielectric switches.

Received 17th May 2024,
Accepted 6th July 2024

DOI: 10.1039/d4qi01243g

rsc.li/frontiers-inorganic

Introduction

Dielectric switches, as a unique type of electrically polarizable materials, are capable of reversibly modulating an electrical signal between two distinct dielectric states triggered by external thermal, mechanical, or optical stimuli. Such a reconfigurable function renders them ideal candidates for use in smart stimulus-responsive system, sensing technology, and signal storage.[1–10] While mechanically activated dielectric switches, known as piezoelectrics, have played crucial roles in contemporary electrical and electronic devices, their temperature-driven counterparts are less developed but have aroused a growing interest in recent years.[11–24]

From the perspective of polarization mechanism, temperature-driven dielectric switching in crystalline molecule-based materials usually stems from the variation of a dipole unit from frozen to thermally activated, or an alteration of its rotational dynamics that is often accompanied by a structural phase transition. The switching temperatures (T_s) in most of these switches are restrictively fixed at the phase transition temperatures. Nevertheless, for practical application, dielectric switches with multiple and/or adjustable T_s are more desirable yet challenging to achieve. To overcome this deficiency, we noticed that cage-like hybrid double perovskites (especially the rare-earth double perovskites),[25–39] as a well-known class of phase-change compounds, may be good targets for the design of temperature-tunable multiple dielectric switches. As shown in Chart 1, three combined approaches may be implemented to afford such switches in the hybrid rare-earth perovskite system. Firstly, a guest cation with flexible and diverse conformations, regulated by different degrees of rotational energy barrier in the cage-confined space, is more preferable to exhibit hierarchical molecular dynamics. Also, a sphere-like characteristic is considerable, which is conducive to structural phase transition according to the "quasi-spherical theory" proposed by Xiong *et al.*[40,41] Secondly, we aim to further tune the T_s through the lanthanide contraction effect of rare-earth ions, a systematic decrease in ionic radii across the lanthanide series.[42–45] Thirdly, considering the similarity of lanthanide ions, an effortless solutionizing strategy, *i.e.*, the doping of

[a]*College of Chemistry and Chemical Engineering, Jiangxi Normal University, Nanchang 330022, China. E-mail: ziyidu@gmail.com*
[b]*MOE Key Laboratory of Bioinorganic and Synthetic Chemistry, GBRCE for Functional Molecular Engineering, School of Chemistry, IGCME, Sun Yat-Sen University, Guangzhou 510275, China. E-mail: zhangwx6@mail.sysu.edu.cn*
[c]*Graduate School of Environmental Science, Hokkaido University, Sapporo 060-0810, Japan. E-mail: huangrk@es.hokudai.ac.jp*
[d]*Research Institute for Electronic Science (RIES), Hokkaido University, Sapporo 001-0020, Japan*

†Electronic supplementary information (ESI) available. CCDC 2353399, 2353482–2353484 and 2353693–2353695. For ESI and crystallographic data in CIF or other electronic format see DOI: https://doi.org/10.1039/d4qi01243g

‡These authors contributed equally.

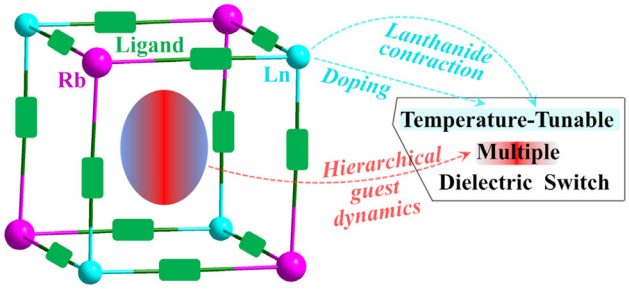

Chart 1 Triply combined approach for the design of temperature-tunable multiple dielectric switch in cage-like hybrid rare-earth perovskites.

different rare-earth ions within these rare-earth perovskites, can also be employed to effectively tune the T_s.

Till now, only one single phase transition at most was observed for the reported cage-like hybrid rare-earth perovskites.[34–39] The reason may be due to the lack of conformational flexibility/diversity for the incorporated ammonium guests within these perovskites. Here we adopt $(Me_2HC–NHMe_2)^+$, *i.e.* $(i\text{-}PrNHMe_2)^+$ cation, which exhibits a flexible "C–N" core with a highly variable torsion angle $\theta_{H–N–C–H}$, as a conformationally flexible sphere-like guest,[46–48] to induce stepwise phase transitions in the hybrid rare-earth perovskite system. With this strategy, we synthesized a series of hybrid rare-earth perovskites composed of trivalent rare-earth ions and monovalent alkali Rb^+ ions, namely, $(i\text{-}PrNHMe_2)_2[RbLn(NO_3)_6]$ (Ln = La, **1**; Ce, **2**; Nd, **3**; Sm, **4**). Further studies revealed that **1** is a two-step dielectric switch and the isomorphic **2–4** function as three-step dielectric switches due to the hierarchical guest dynamics, which are sensitively tuned by lanthanide contraction as well as lanthanide doping.

Results and discussion

Thermal analyses of 1–4

The thermogravimetric analyses of **1–4** show that they are stable up to at least 450 K (Fig. S1†). DSC measurement was used to detect the possible phase transitions. As shown in Fig. 1, the DSC curves of **1** exhibit a pair of endothermic/exothermic peaks at heating/cooling run, revealing that it undergoes a reversible phase transition at T_1. For convenience, we label the phases below/above T_1 as **1α/1γ** phase, respectively. In contrast, two reversible phase transitions at T_1 and T_2 are recorded for all of the homogeneous **2–4**. In other words, a metastable intermediate phase emerges in **2–4**. For convenience, we label the phases of **2–4** below T_1 as **α** phase, between T_1 and T_2 as **β** phase, and above T_2 as **γ** phase. As shown in Table S1,† the phase transition temperatures of T_1 for **1–4** are roughly similar (282–287 K for heating process), while those of T_2 for **2–4** on heating run decrease from 258 K to 229 K, and further to 206 K. For all of these transitions, they belong to a first-order phase transition, with moderate thermal hysteresis

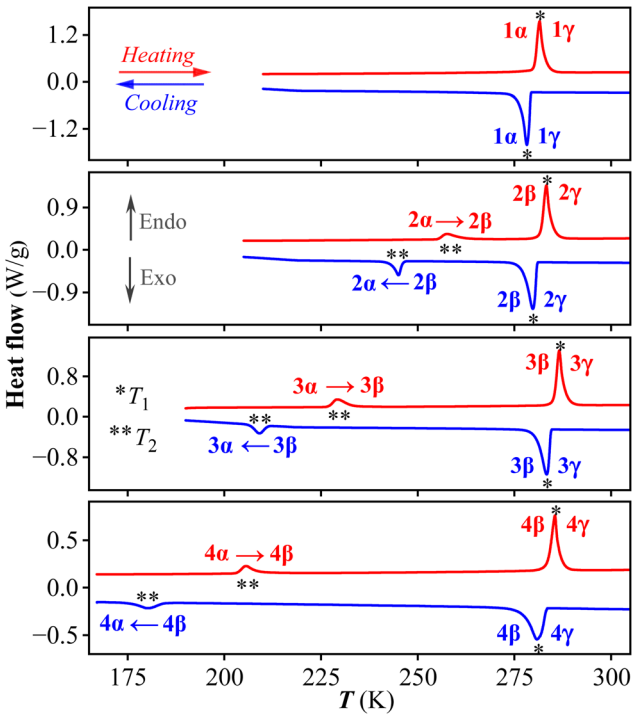

Fig. 1 The DSC measurement of **1–4** in a heating–cooling cycle.

of ΔT_1 between the heating and cooling runs for **1–4** (*ca.* 3–4 K) and relatively large thermal hysteresis of ΔT_2 for **2–4** (about 13, 20, and 26 K, respectively).

Stepwise phase transitions of 2 and its crystal structures in three phases

To understand the phase transitions detected by DSC measurement, single-crystal X-ray diffraction was performed for **1–4**. It was uncovered that **1–4** are isomorphous and the last three have similar phase transition behavior (note: different to **2–4** which contain **α/β/γ** three phases, **1** only features **α/γ** two phases), hence here only the structure of **2** is discussed in detail as a representative. Compound **2** crystallizes in the space group $C2/m$ at 173 K (**α** phase), $R\bar{3}m$ at 273 K (**β** phase), and $Fm\bar{3}m$ at 293 K (**γ** phase), respectively (Table S2†). The crystal structure of **2** can be roughly described as an organic–inorganic hybrid double perovskite, with a general formula of $A_2(B'B'')Y_6$ (A = monovalent organic cation, B′/B″ = monovalent/trivalent metal cation, arranged orderly and alternately over two types of B sublattices, and Y = monovalent anionic bridging ligand), which is topologically similar to $(RM_3HQ)_2RbLa(NO_3)_6$ reported by Zhang and Ye, *et al.*[34] The Ce^{3+} center here is twelve-coordinated by six bidentate chelating NO_3^- ions, while the Rb^+ ion is surrounded by six O atoms from six NO_3^- ions. For each NO_3^- ion, it bidentately chelates with one Ce^{3+} ion and further bridges with a Rb^+ ion through its third O atom, which acts as an end-to-end bridging ligand between the Ce^{3+} and Rb^+ ions. The interconnection of Ce^{3+} and Rb^+ ions by the bridging NO_3^- ligands leads to a three-dimensional cage-like framework, with per $(i\text{-}PrNHMe_2)^+$

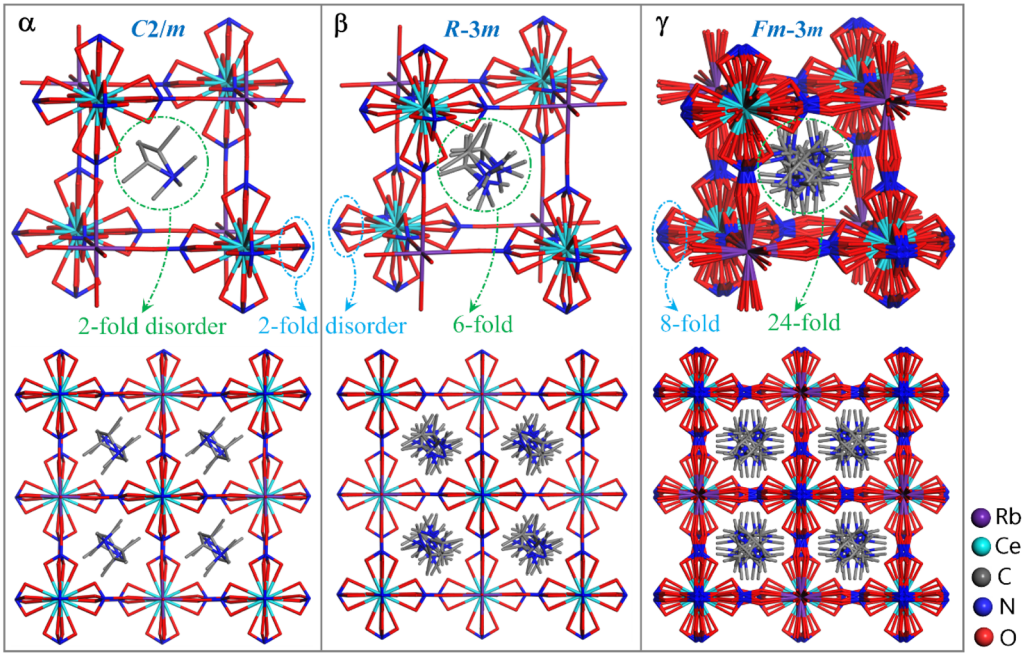

Fig. 2 Cage units and packing diagrams of **2** at 173 K (α phase), 273 K (β phase), and 293 K (γ phase), respectively. The $(i\text{-PrNHMe}_2)^+$ and NO_3^- ions exhibit varying degrees of disorder in all phases. H atoms are omitted for clarity.

cation residing in a cage unit (Fig. 2). Each $[Ce_{0.5}Rb_{0.5}(NO_3)_3]^-$ cage unit is enclosed by twelve Ce–(NO_3)–Rb fragments, with a length of ~7.0 Å.

The driving force for the structural phase transition of **2** can mainly be attributed to the different degrees of disorder of the $(i\text{-PrNHMe}_2)^+$ and NO_3^- ions in its three phases. In **2α**, **2β** and **2γ** phases, the $(i\text{-PrNHMe}_2)^+$ ion features 2-, 6- and 24-fold disorder, respectively, while the NO_3^- ion exhibits 2-, 2- and 8-fold disorder, respectively (Fig. 2). The synergic disorder of these components leads to symmetry breaking in the perovskite-like structure, with the total symmetric elements of the crystallographic point group increasing from 4 (E, C_2, i, σ_h) in **2α** phase to 12 (E, $2C_3$, $3C_2$, i, $2S_6$, $3\sigma_v$) in **2β** phase, and further to 48 (E, $8C_3$, $3C_2$, $6C'_2$, $6C_4$, i, $8S_6$, $3\sigma_h$, $6\sigma_d$, $6S_4$) in **2γ** phase. Correspondingly, the occupancy factors for both Ce^{3+} and Rb^+ ions in the three phases are reduced from 1/4 (**2α** phase) to 1/12 (**2β** phase), and further to 1/48 (**2γ** phase). Each pair of the 2-fold disordered $(i\text{-PrNHMe}_2)^+$ ions in **2α** phase are related by a mirror symmetry, and six of the 6-fold disordered $(i\text{-PrNHMe}_2)^+$ ions in **2β** phase are related by C_{3v} symmetry, while twenty-four of the 24-fold disordered $(i\text{-PrNHMe}_2)^+$ ions in **2γ** phase are related by T_d symmetry. Overall, the organic–inorganic hybrid hetero-metallic perovskite structures in **2α**, **2β** and **2γ** phases are characterized by symmetries of C_{2h}, D_{3d} and O_h, respectively.

Multiple dielectric switching of 2 and the related mechanism

The above-mentioned varied disordered state of the guest $(i\text{-PrNHMe}_2)^+$ ion in **2** upon thermal stimulation strongly signifies that it is swingable or rotatable in the cage-confined space, which should cause a sensitive dielectric response owing to its changing orientation polarization under an AC electric field. We thus performed the variable-temperature dielectric measurement on the powder-pressed pellet sample of **2**, with its complex permittivity ε^* ($\varepsilon' - i\varepsilon''$, where ε' and ε'' are the real and imaginary parts, respectively) being measured over a frequency range from 0.5 to 1000 kHz. As shown in Fig. 3, from 100 to 340 K, the dielectric constants under all test frequencies switch from a dielectric-inactive region **I** (roughly below 153 K, **2α** phase) to a dielectric-active region **II** (153–253 K, **2α** phase), followed by another dielectric-inactive region **III** (253–285 K, **2β** phase), and culminating in a new dielectric-active state **IV** (above 285 K, **2γ** phase). It is worthy of note that the dielectric-inactive phenomena in regions **I** and **III** are distinct in essence (*vide infra*). In region **II**, the ε' and ε'' both show notable frequency dispersion, which can be explicated in terms of the dielectric relaxation of a swingable $(i\text{-PrNHMe}_2)^+$ ion. The peak maxima of ε'' are recorded at the increasing temperatures (T_{peak}) from 180 to 248 K for the increasing f "0.5 → 250 kHz". Overall, a seldom observed pattern of multiple dielectric switching characterized by the transitions of "Low ↔ High ↔ Low ↔ High" was revealed in **2**.

From the perspective of molecular dynamics, region **I** is indicative of a "frozen" state for the $(i\text{-PrNHMe}_2)^+$ ion, where its motion is significantly restricted. In contrast, region **II** corresponds to a swingable $(i\text{-PrNHMe}_2)^+$ ion between bistable states, exhibiting an increase in motion frequency from 10^1 to 10^6 as temperature rises. For region **III**, the $(i\text{-PrNHMe}_2)^+$ ion is in a more disordered, swing state, crystallographically characterized by 6-fold disorder. This state is marked by a motion frequency substantially exceeding 10^6,

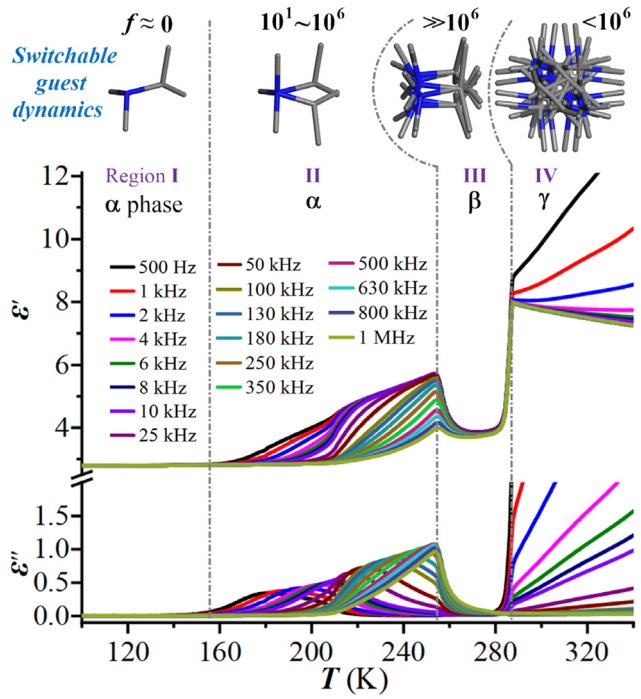

Fig. 3 Temperature-dependent ε' and ε'' of **2** at various AC frequencies and the related switchable guest dynamics.

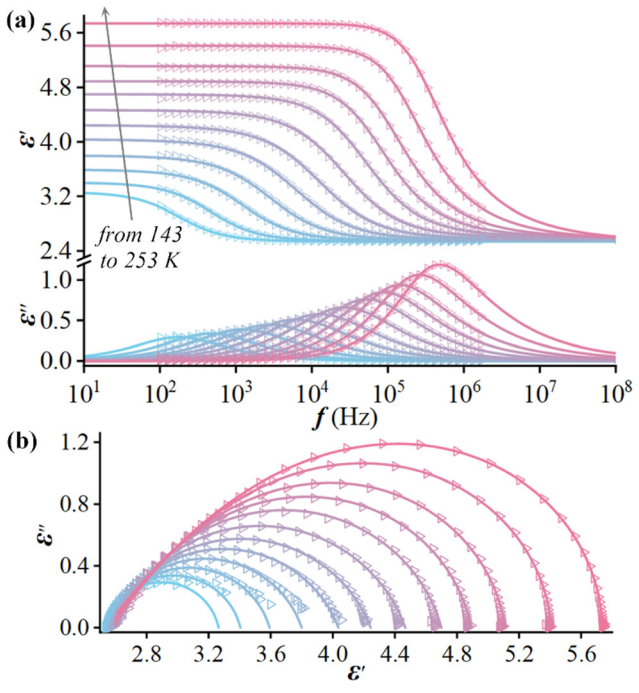

Fig. 4 Frequency-dependent ε' and ε'' for **2** at selected temperatures from 143 to 253 K in an increasing step of 10 K (a), and the Cole–Cole diagrams are plotted as a series of arcs to show the relationship between ε' and ε'' (b). Solid curves represent the fit of the experimental data to the Havriliak–Negami equation.

a rate too rapid to be responded by the applied AC frequency. Transitioning into region **IV**, the $(i\text{-PrNHMe}_2)^+$ ion enters a fully rotating state, distinguished crystallographically by a 24-fold disorder. At this stage, the alteration in motion mode results in an increased rotational energy barrier, consequently reducing the motion frequency to below 10^6. This change brings the $(i\text{-PrNHMe}_2)^+$ ion back to a dielectric responsible state.

To deeply characterize the dielectric relaxation in region **II**, the ε^* was further measured as a function of f at a series of constant temperatures. The results uncover that there exists a single relaxation process, which can be fitted by a Havriliak–Negami equation:[49] $\varepsilon^* = \varepsilon_\infty + (\varepsilon_s - \varepsilon_\infty)/\{[1 + (i\omega\tau)^{(1-\alpha)}]^\beta\}$ $(0 \leq \alpha, \beta \leq 1)$, where ω is the angular frequency, τ is the relaxation time, α/β are related to the distribution of relaxation time, and $\varepsilon_s/\varepsilon_\infty$ are the low/high-frequency limits of dielectric permittivity, respectively. The resultant fitted parameters (Table S6†) and fitted curves (Fig. 4a) match well with the experimental data.

The parameter ε_∞, as the contribution of ionic polarization apart from electronic polarization, almost remains constant upon heating, suggesting that the electrostatic binding force between the cage-like $[RbCe(NO_3)_6]^{2-}$ framework and the embedded $(i\text{-PrNHMe}_2)^+$ ion changes little with rising temperature. The relaxation in region **II** is mainly attributed to the dipolar polarization of the dynamically disordered $(i\text{-PrNHMe}_2)^+$ ion. The increasing ε_s upon heating means that the continuously strengthened molecular thermal motion of the disordered $(i\text{-PrNHMe}_2)^+$ ion promotes the dipolar polarization. The value of α is roughly in the range of 0.1–0.2, suggesting a polarization mechanism with non-single relaxation time, and the value of β gradually deviates from 1.0 above 213 K can be mainly ascribed to the thermally enhanced interaction between the host $[RbCe(NO_3)_6]^{2-}$ framework and the guest $(i\text{-PrNHMe}_2)^+$ ion. Upon heating, the relaxation time τ turns short from 8.9×10^{-4} s at 143 K to 9.0×10^{-7} s at 243 K. The relaxation process can also be intuitively demonstrated by the so-called Cole–Cole formalisms (ε' *vs.* ε'') drawn in an Argand diagram, which are plotted as a series of arcs (Fig. 4b). The relaxation times τ obey the Arrhenius equation: $1/\tau = \omega_0 \exp[-E_a/(k_B T)]$, where ω_0 is a pre-exponential factor, E_a is an activation energy, and k_B is the Boltzmann constant. By linearly fitting the plots of $1000/T$ *vs.* $\ln(1/\tau)$ (Fig. S4†), an ω_0 of 2.6×10^{10} s^{-1}, and an E_a of 0.21 eV, were estimated for this relaxation. Such a relatively low energy barrier can mainly be ascribed the near-spherical $(i\text{-PrNHMe}_2)^+$ ion with a flexible "C–N" core.

Temperature-tunable dielectric switching regulated by lanthanide contraction or rare-earth doping

As implied in the above-mentioned DSC measurement, the T_s of the multiple dielectric switch **2** may be sensitively tuned by lanthanide contraction. Thus, a detailed comparison of the temperature-dependent multiple dielectric switches of **1–4** at various AC frequencies is performed and depicted in Fig. 5. With a steady decrease in the size (ionic radii) of the rare-earth

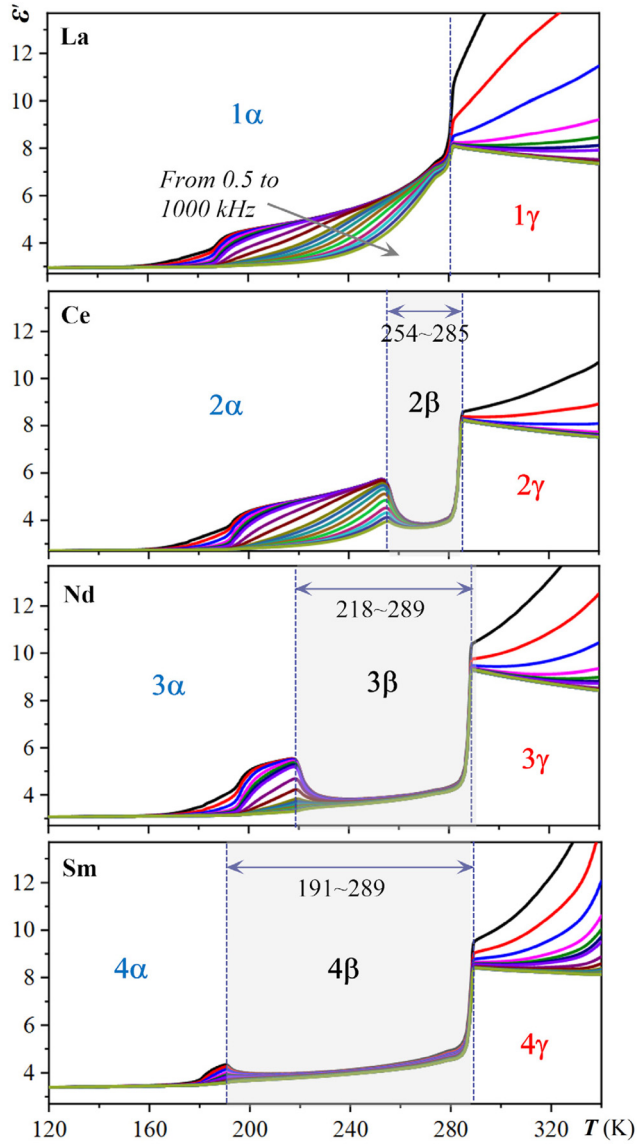

Fig. 5 Comparison of the temperature-dependent multiple dielectric switches **1–4** at various AC frequencies. For display detail, see Fig. 3.

ions from **1** to **4** (*i.e.*, 1.061, 1.034, 0.0995, and 0.0964 Å for La^{3+}, Ce^{3+}, Nd^{3+}, Sm^{3+}, respectively), a dramatic confined effect is realized in such a hybrid rare-earth perovskite system. The temperature ranges of metastable **β** phase in **2–4** increase from 254–285 K to 218–289 K, and to 191–289 K. Overall, the utilizing of lanthanide contraction allows for the fine-tuning of T_s.

To further tune the T_s of the multiple dielectric switches within these hybrid rare-earth perovskites, exemplary lanthanide doping experiments between **1** and **3** are performed in a wide range of doping ratio. The PXRD measurements of these doping samples show that continuous solid solutions can be readily formed between them (Fig. S6†). The comparison of the DSC curves (Fig. S3†) as well as the variable-temperature dielectric spectra for **3** and its lanthanum-doped solid solutions (Fig. S4†) clearly illustrated that the phase transition temperature T_1 in **3** can be continuously tuned *via* lanthanum doping (for instance, from 218 K in **3** to 266 K in $(i\text{-PrNHMe}_2)_2[Rb(La_{0.5}Nd_{0.5})(NO_3)_6]$, while the T_2 has hardly changed). Such distinct effects can be explained as follows: in the high-temperature phase, the nitrate ligand is highly disordered with significant atomic thermal vibrations, which results in a relatively loose perovskite-like coordination framework, making the influence of rare-earth ion radii on the structure less noticeable. For the low-temperature phase, the atomic thermal vibrations of nitrate ligand are weakened substantially. Consequently, the perovskite-like coordination framework becomes more inflexible, which should be sensitively influenced by the size of rare-earth ion. Thus, the effect of lanthanide contraction or doping is more pronounced for the low-temperature phase than the high-temperature one.

Multiaxial ferroelasticity in 1–4

The phase transition from **1γ** to **1α** is theoretically ferroelastic, characterized by the Aizu notation "$m\bar{3}mF2/m$",[50] with up to 12 equivalent ferroelastic directions. To investigate its ferroelastic characteristics, polarized light microscopy was employed to examine the variable-temperature evolution of the ferroelastic domain on a single crystal of **1**. Due to the birefringence effect, the ferroelastic domain can exhibit contrasting light and dark patterns under orthogonally polarized light. As shown in Fig. 6a, in the paraelastic **1γ** phase, no observable domains are present at 300 K. However, upon cooling to the **1α** phase at 240 K, the image becomes darker, indicating the emergence of multiple domain patterns. Similarly, the transitions of **β** → **α** and **γ** → **β** in **2**, **3** and **4** are also theoretically ferroelastic, with Aizu notations of "$\bar{3}mF2/m$" and "$m\bar{3}mF\bar{3}m$", respectively, and the number of equivalent ferroelastic directions for these transitions are **3** and **4**, respectively. Fig. 6b–d demonstrate that in the paraelastic **γ** phase at 300 K, no domains are visible. Cooling to the **β** phase leads to the appearance of ferroelastic domains. Further cooling to the **α** phase darkens the image under the polarizing microscope owing to increased domain formation. Overall, the thermal reversibility of these domain patterns during a consecutive cooling–heating cycle confirms the presence of ferroelasticity in the **α** and **β** phases of these hybrid rare-earth perovskites.

Experimental

Materials and methods

All chemicals were obtained from commercial sources and used without further purification. FT-IR spectra were recorded on a Nicolet 6700 FT-IR spectrometer using KBr pellets from 4000 to 400 cm^{-1}. Powder X-ray diffraction (PXRD) patterns (Cu-Kα) were collected on a Rigaku MiniFlex600 θ–2θ diffractometer. Thermogravimetric analysis (TGA) was carried out on a TA Q50 system at a heating rate of 10 °C min^{-1} under a dinitrogen atmosphere. Differential scanning calorimeter (DSC) measurements were performed by heating and cooling the powder sample on a TA DSC 250 instrument, at a rate of 10 °C

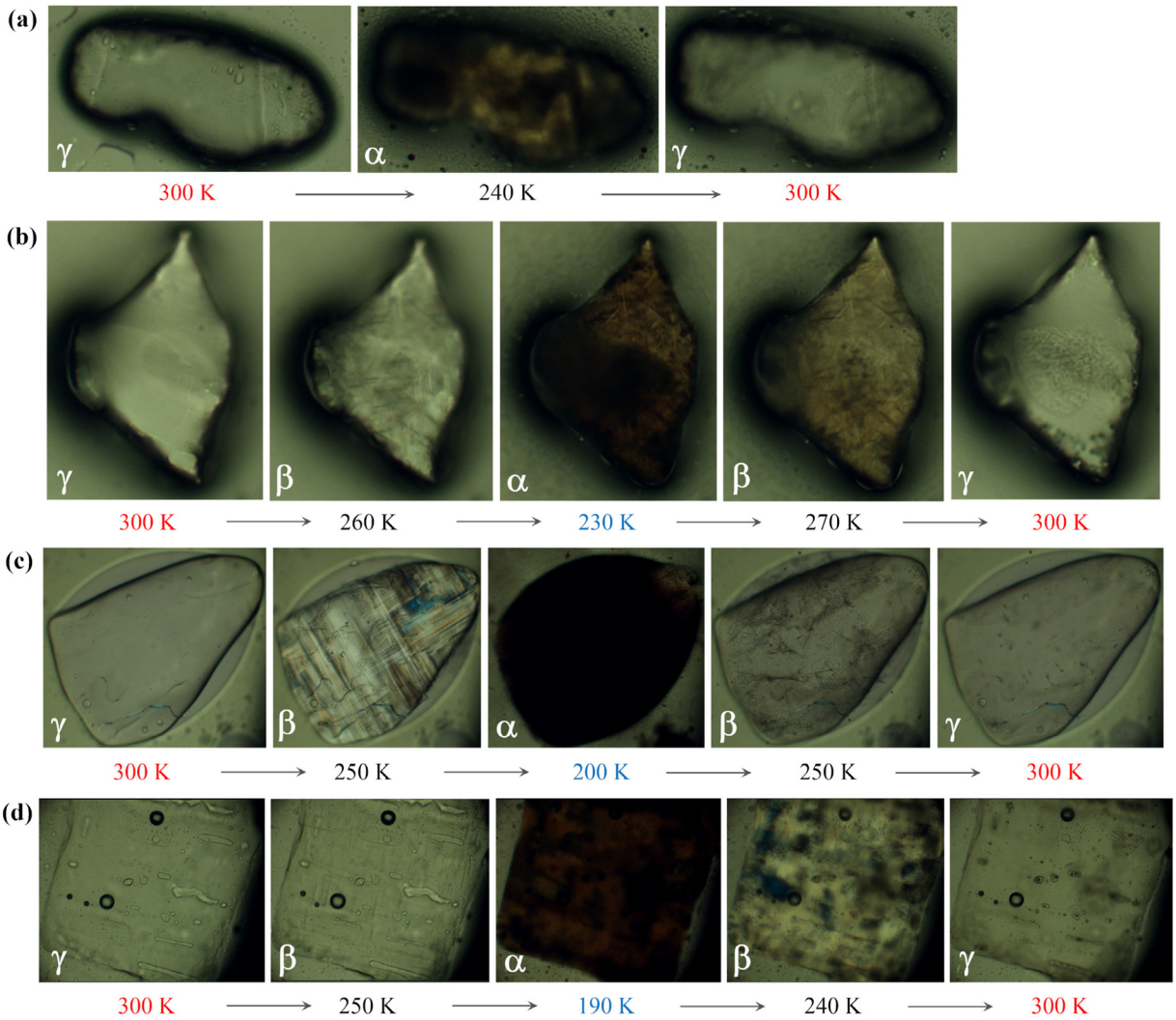

Fig. 6 Variable-temperature evolution of the ferroelastic domains for **1** (a), **2** (b), **3** (c) and **4** (d), respectively, observed under polarization microscope. Crystal sizes: 1.4 × 0.4 × 0.2 mm for **1**, 1.6 × 0.7 × 0.3 mm for **2**, 2.2 × 1.3 × 0.5 mm for **3**, and 2.5 × 2.3 × 0.3 mm for **4**.

min^{-1}. The complex permittivities were measured under a nitrogen gas atmosphere, using a Tonghui TH2828A LCR meter in a Mercury iTC cryogenic environment controller of Oxford Instrument, and the samples were ground and pressed into tablets under a pressure of 3 MPa. Energy dispersive X-ray spectroscopy (EDS) elemental mapping was carried out on a ZEISS EVO10 scanning electron microscope (SEM). Photoluminescence analysis was performed on an Edinburgh FLS980 fluorescence spectrometer.

Syntheses of 1–4

In a 50 mL beaker, $RbNO_3$ (5.0 mmol), $La(NO_3)_3{\cdot}6H_2O$ (5.0 mmol) and (i-PrNHMe$_2$)NO_3 (10.0 mmol) were dissolved in H_2O (18 mL). The resultant clear solution was allowed to stand at room temperature. Three days later, colorless block-shaped crystals of **1** were deposited from the solution, in a *ca.* 87% yield based on La. IR data (KBr, cm^{-1}): 3424(s), 2984(m), 2738(m), 2369(m), 1635(s), 1380(vs), 1335(s), 1156(m), 1039(m), 931(m), 826(s), 742(m). When a similar procedure was performed but with $Ce(NO_3)_3{\cdot}6H_2O$/$Nd(NO_3)_3{\cdot}6H_2O$/$Sm(NO_3)_3{\cdot}6H_2O$ in place of $La(NO_3)_3{\cdot}6H_2O$, block-shaped crystals of **2**/**3**/**4** were obtained. The PXRD for the bulky crystals of them indicated that their experimental patterns match well with the simulated ones (Fig. S5†).

Syntheses of the molecular solid solutions of 1 and 3

The slow evaporation of the aqueous solution of **1** and **3** at 308 K, in the mixing ratios of $x:(1-x)$, afforded the molecular solid solutions (i-PrNHMe$_2$)$_2$[Rb(La$_x$Nd$_{1-x}$)(NO$_3$)$_6$] in 100% yield, where x = 0.2, 0.35 and 0.5, respectively. The PXRD for these doping samples displayed that their experimental patterns match well with the patterns of **1** and **3** (Fig. S6†). The relative contents of La and Nd in these molecular solid solutions were semi quantitatively checked by SEM-EDS (Fig. S7†), showing that the ratios of La and Nd in them are roughly equivalent to the proportion of the starting experimental materials

(for x = 0.20, 0.35, and 0.50, the corresponding $x_{mapping}$ are about 0.26, 0.40 and 0.55, respectively).

Luminescent property of 4

The solid-state luminescent spectra of **2–4** were investigated at room temperature. Under excitation of 403 nm, compound **4** displays the characteristic emission bands for the samarium (III) ion (Fig. S8†): two sharp emission bands at 561 nm ($^4G_{5/2} \rightarrow {}^6H_{5/2}$) and 595 nm ($^4G_{5/2} \rightarrow {}^6H_{7/2}$), respectively, and a middle emission band at 641 nm ($^4G_{5/2} \rightarrow {}^6H_{9/2}$) as well as a weak band at 704 nm ($^4G_{5/2} \rightarrow {}^6H_{11/2}$). For **2** and **3**, only somewhat weak emissions were detected.

Single-crystal X-ray crystallography

The *in situ* variable-temperature single-crystal X-ray diffraction intensities for **2** at 293/273/173 K and those for **1**/**3**/**4** at 293 K were collected on a Rigaku synergistic diffractometer equipped with a graphite-monochromated Mo-Kα radiation (λ = 0.71073 Å), respectively. Absorption corrections were applied by using multi-scan program CrysAlisPro.[51] The structures were solved by direct methods and refined using full-matrix least-squares technique with the SHELX program package.[52] All hydrogen atoms were generated geometrically. Crystallographic data and structural refinements for **2** at 293/273/173 K, **1** at 293/223 K, and **3**/**4** at 293 K are summarized in Tables S2 and S3,† respectively. Selected bond lengths are listed in Tables S4 and S5,† respectively. CCDC numbers 2353399, 2353482–2353484, and 2353693–2353695† contain the supplementary crystallographic data for **1–4** in this paper. Note: the collection of low-temperature crystallographic data for **3** and **4** failed because the peaks of single-crystal diffraction became complicatedly multiple (from single to more than 6) after phase transition. This occurrence may be caused by the internal stress during the multiaxial ferroelastic phase transition, which gradually increased as the cage's size decreased progressively from **1** to **4**.

Conclusion

In summary, our study on a series of unique cage-like hybrid rare-earth perovskites (i-PrNHMe$_2$)$_2$[RbLn(NO$_3$)$_6$] (Ln = La, Ce, Nd or Sm), has successfully demonstrated their potential as multiple dielectric switches with flexible temperature tunability. The confinement of a conformationally flexible sphere-like guest, the (i-PrNHMe$_2$)$^+$ cation, within the perovskite framework initiates hierarchical guest dynamics, facilitating stepwise phase transitions and enabling multiple switching states that alternate between "Low ↔ High ↔ Low ↔ High" with heating. The adaptability of the switching temperatures can be precisely modulated through lanthanide contraction and doping with different lanthanide ions, highlighting their prospective utility in responsive electronic devices. Furthermore, the observation of multiaxial ferroelasticity in these compounds adds to their functional versatility. Overall, the unique hybrid perovskite system in this study offers an interesting platform for the exploitation of temperature-tunable multiple dielectric switches.

Data availability

The data are available from the corresponding author on reasonable request. The ESI† contains the crystallographic data and characterization details for the title compounds.

Conflicts of interest

The authors declare no conflict of interest.

Acknowledgements

This work was supported by the National Natural Science Foundation of China (21971091 and 22071273), the Natural Science Foundation of Jiangxi Province (20224ACB203002), Guangzhou Science and Technology Programme (2024A04J6499), and Fundamental Research Funds for the Central Universities, Sun Yat-Sen University (23lgzy001).

References

1 Z. G. Ye, *Handbook of Advanced Dielectric, Piezoelectric and Ferroelectric Materials*, Woodhead Publishing Ltd, Cambridge, 2008.
2 Y. Poplavko and Y. Yakymenko, *Functional Dielectrics for Electronics: Fundamentals of Conversion Properties*, Woodhead Publishing Ltd, Cambridge, 2020.
3 W. Zhang, H. Y. Ye, R. Graf, H. W. Spiess, Y. F. Yao, R. Q. Zhu and R. G. Xiong, Tunable and Switchable Dielectric Constant in an Amphidynamic Crystal, *J. Am. Chem. Soc.*, 2013, **135**, 5230.
4 J. Harada, M. Ohtani, Y. Takahashi and T. Inabe, Molecular Motion, Dielectric Response, and Phase Transition of Charge-Transfer Crystals: Acquired Dynamic and Dielectric Properties of Polar Molecules in Crystals, *J. Am. Chem. Soc.*, 2015, **137**, 4477.
5 N. F. Polizzi, M. J. Eibling, J. M. Perez Aguilar, J. Rawson, C. J. Lanci, H. C. Fry, D. N. Beratan, J. G. Saven and M. J. Therien, Photoinduced Electron Transfer Elicits a Change in the Static Dielectric Constant of a de Novo Designed Protein, *J. Am. Chem. Soc.*, 2016, **138**, 2130.
6 H. Y. Ye, W. Q. Liao, Q. Zhou, Y. Zhang, J. Wang, Y. M. You, J. Y. Wang, Z. N. Chen, P. F. Li, D. W. Fu, S. D. Huang and R. G. Xiong, Dielectric and ferroelectric sensing based on molecular recognition in Cu(1,10-phenlothroline)$_2$SeO$_4$·(diol) systems, *Nat. Commun.*, 2017, **8**, 14551.
7 W. Q. Liao, D. Zhao, Y. Y. Tang, Y. Zhang, P. F. Li, P. P. Shi, X. G. Chen, Y. M. You and R. G. Xiong, A molecular perovs-

kite solid solution with piezoelectricity stronger than lead zirconate titanate, *Science*, 2019, **363**, 1206.
8 Y. Zhang, X. J. Song, Z. X. Zhang, D. W. Fu and R. G. Xiong, Piezoelectric Energy Harvesting Based on Multiaxial Ferroelectrics by Precise Molecular Design, *Matter*, 2020, **2**, 697.
9 Y. Y. Tang, J. C. Liu, Y. L. Zeng, H. Peng, X. Q. Huang, M. J. Yang and R. G. Xiong, Optical Control of Polarization Switching in a Single-Component Organic Ferroelectric Crystal, *J. Am. Chem. Soc.*, 2021, **143**, 13816.
10 H. Y. Zhang, Y. Y. Tang, Z. X. Gu, P. Wang, X. G. Chen, H. P. Lv, P. F. Li, Q. Jiang, N. Gu, S. Ren and R. G. Xiong, Biodegradable ferroelectric molecular crystal with large piezoelectric response, *Science*, 2024, **383**, 1492.
11 J. Y. Liu, S. Y. Zhang, Y. Zeng, X. Shu, Z. Y. Du, C. T. He, W. X. Zhang and X. M. Chen, Molecular Dynamics, Phase Transition and Frequency-Tuned Dielectric Switch of an Ionic Co-Crystal, *Angew. Chem., Int. Ed.*, 2018, **57**, 8032.
12 P. Meng, Y. Wu, Q. Zhang, G. Cheng, X. Wu and R. Zheng, Room Temperature Dielectric Pulse Effect in Organic Mixtures, *Adv. Funct. Mater.*, 2018, **28**, 1801421.
13 T. Zhang, L. Chu, Z. Zhang, J. Li, W. Zhang, P. Shi, Q. Ye and D. W. Fu, Full-temperature covered switching material with triple optic-dielectric states in a lead-free hybrid perovskite, *Sci. China Mater.*, 2020, **63**, 2281.
14 Z. X. Zhang, C. Y. Su, J. Li, X. J. Song, D. W. Fu and Y. Zhang, Ferroelastic Hybrid Bismuth Bromides with Dual Dielectric Switches, *Chem. Mater.*, 2021, **33**, 5790.
15 Y. Wang, T. Zhang, M. M. Lun, F. L. Zhou, D. W. Fu and Y. Zhang, Halogen regulation triggers NLO and dielectric dual switches in hybrid compounds with green fluorescence, *Inorg. Chem. Front.*, 2021, **8**, 4230.
16 Y. Gong, Z. Li, H. Li, W. Wu, W. Zhou, J. Zhao, C. He and M. Jiang, Ultra-Tough Room-Temperature Dielectric Switching Ionic Gels with Long-Cycle Stability, *Adv. Funct. Mater.*, 2022, **32**, 2207452.
17 T. Shao, H. F. Ni, C. Y. Su, Q. Q. Jia, L. Y. Xie, D. W. Fu and H. F. Lu, Integrated Reversible Thermochromism, High *T*C, Dielectric Switch and Narrow Band Gap in One Multifunctional Ferroic, *Chem. – Eur. J.*, 2022, **28**, e202202533.
18 M. Liberka, M. Zychowicz, J. Hooper, K. Nakabayashi, S. Ohkoshi and S. Chorazy, Synchronous Switching of Dielectric Constant and Photoluminescence in Cyanidonitridorhenate-Based Crystals, *Angew. Chem., Int. Ed.*, 2023, **62**, e202308284.
19 H. Pan, Z. Tian, M. Acharya, X. Huang, P. Kavle, H. Zhang, L. Wu, D. Chen, J. Carroll, R. Scales, C. J. G. Meyers, K. Coleman, B. Hanrahan, J. E. E. Spanier and L. W. W. Martin, Defect-Induced, Ferroelectric-Like Switching and Adjustable Dielectric Tunability in Antiferroelectrics, *Adv. Mater.*, 2023, **35**, 2300257.
20 Y. Gong, J. Zhao, Z. Li, J. Huang, Y. Zhang, L. Dong, C. Xiong and M. Jiang, Unparalleled Dielectric-Switching Effects Caused by Dual Polarization Synergy, *Adv. Funct. Mater.*, 2023, **33**, 2214544.
21 J. Guo, S. Y. Zhang, C. H. Zeng, Z. G. Zhou, M. Xie, Z. Y. Du, C. T. He, W. X. Zhang and X. M. Chen, Temperature-Tuned Variable Confined Space for Modulating Dipolar Polarization of a Disc-Shaped Ammonium Ion, *J. Phys. Chem. Lett.*, 2023, **14**, 8009.
22 W. J. Wei, H. Q. Gao, X. H. Luo and Y. Z. Tang, Dielectric Relaxation and Dielectric Switching Behaviors in (N, N-Diisopropylethylamine) Tetrachloroantimonate(III), *Chem. – Eur. J.*, 2023, **29**, e202202916.
23 T. Y. Ju, C. D. Liu, C. C. Fan, B. D. Liang, C. Y. Chai and W. Zhang, Halogen Substitution Regulates High Temperature Dielectric Switch in Lead-Free Chiral Hybrid Perovskites, *Chem. – Eur. J.*, 2024, **30**, e202303415.
24 P. Wang, X. Li, H. Ye, Q. Guan, Y. Wang, Y. Geng, C. Zhang, H. Li and J. Luo, Durable dielectric switching and photoresponsivity in a Dion-Jacobson hybrid perovskite semiconductor, *Inorg. Chem. Front.*, 2024, **11**, 2436.
25 C. Shi, C. H. Yu and W. Zhang, Predicting and Screening Dielectric Transitions in a Series of Hybrid Organic-Inorganic Double Perovskites via an Extended Tolerance Factor Approach, *Angew. Chem., Int. Ed.*, 2016, **55**, 5798.
26 F. Wei, Z. Deng, S. Sun, F. Xie, G. Kieslich, D. M. Evans, M. A. Carpenter, P. D. Bristowe and A. K. Cheetham, The synthesis, structure and electronic properties of a lead-free hybrid inorganic-organic double perovskite $(MA)_2KBiCl_6$ (MA = methylammonium), *Mater. Horiz.*, 2016, **3**, 328.
27 W. J. Xu, Z. Y. Du, W. X. Zhang and X. M. Chen, Structural phase transitions in perovskite compounds based on diatomic or multiatomic bridges, *CrystEngComm*, 2016, **18**, 7915.
28 W. Li, Z. Wang, F. Deschler, S. Gao, R. H. Friend and A. K. Cheetham, Chemically diverse and multifunctional hybrid organic-inorganic perovskites, *Nat. Rev. Mater.*, 2017, **2**, 16099.
29 X. G. Zhao, D. Yang, J. C. Ren, Y. Sun, Z. Xiao and L. Zhang, Rational Design of Halide Double Perovskites for Optoelectronic Applications, *Joule*, 2018, **2**, 1662.
30 X. Zhang, L. Li, Z. Sun and J. Luo, Rational chemical doping of metal halide perovskites, *Chem. Soc. Rev.*, 2019, **48**, 517.
31 J. Gebhardt and A. M. Rappe, Mix and Match: Organic and Inorganic Ions in the Perovskite Lattice, *Adv. Mater.*, 2019, **31**, 1802697.
32 Y. Zhao, K. Cruse, M. Abdelsamie, G. Ceder and C. M. Sutter Fella, Synthetic approaches for thin-film halide double perovskites, *Matter*, 2021, **4**, 1801.
33 J. Y. Lee, S. Ling, S. P. Argent, M. S. Senn, L. Canadillas Delgado and M. J. Cliffe, Controlling multiple orderings in metal thiocyanate molecular perovskites $A_x\{Ni[Bi(SCN)_6]\}$, *Chem. Sci.*, 2021, **12**, 3516.
34 C. Shi, J. J. Ma, J. Y. Jiang, M. M. Hua, Q. Xu, H. Yu, Y. Zhang and H. Y. Ye, Large Piezoelectric Response in Hybrid Rare-Earth Double Perovskite Relaxor Ferroelectrics, *J. Am. Chem. Soc.*, 2020, **142**, 9634.
35 C. F. Wang, C. Shi, A. Zheng, Y. Wu, L. Ye, N. Wang, H. Y. Ye, M. G. Ju, P. Duan, J. Wang and Y. Zhang,

Achieving circularly polarized luminescence and large piezoelectric response in hybrid rare-earth double perovskite by a chirality induction strategy, *Mater. Horiz.*, 2022, **9**, 2450.

36 Q. Xu, L. Ye, L. P. Miao, C. Shi and Y. Zhang, H/F Substitution Induced Large Increase of *T*C in a 3D Hybrid Rare-Earth Double Perovskite Multifunctional Compound, *Chem. – Eur. J.*, 2022, **28**, e202103913.

37 Z. B. Hu, C. F. Wang, T. T. Sha, C. Shi, L. Ye, H. Y. Ye, Y. Song, Y. M. You and Y. Zhang, An Effective Strategy of Introducing Chirality to Achieve Multifunctionality in Rare-Earth Double Perovskite Ferroelectrics, *Small Methods*, 2022, **6**, 2200421.

38 J. J. Ma, Q. Xu, L. Ye, Q. W. Wang, Z. X. Gong, C. Shi, H. Y. Ye and Y. Zhang, Structural phase transition and dielectric switching in an organic-inorganic hybrid rare-earth double perovskite-type compound: $(DMP)_2LaRb(NO_3)_6$ (DMP = N,N-dimethylpyrrolidinium cation), *J. Rare Earths*, 2022, **40**, 937.

39 Z. Y. Yue, L. Xiang, N. Wang, L. L. Zou, L. P. Miao, H. Y. Ye and C. Shi, Series of Cage-Like Double Perovskite-Type Hybrid Perovskites with Reversible Structural Phase Transition and Switchable Dielectric Constant Property, *Cryst. Growth Des.*, 2023, **23**, 6860.

40 H. Y. Zhang, Y. Y. Tang, P. P. Shi and R. G. Xiong, Toward the Targeted Design of Molecular Ferroelectrics: Modifying Molecular Symmetries and Homochirality, *Acc. Chem. Res.*, 2019, **52**, 1928.

41 H. Y. Liu, H. Y. Zhang, X. G. Chen and R. G. Xiong, Molecular Design Principles for Ferroelectrics: Ferroelectrochemistry, *J. Am. Chem. Soc.*, 2020, **142**, 15205.

42 M. Seitz, A. G. Oliver and K. N. Raymond, The lanthanide contraction revisited, *J. Am. Chem. Soc.*, 2007, **129**, 11153.

43 G. Ferru, B. Reinhart, M. K. Bera, M. O. de la Cruz, B. Qiao and R. J. Ellis, The Lanthanide Contraction beyond Coordination Chemistry, *Chem. – Eur. J.*, 2016, **22**, 6899.

44 G. S. Silva, J. D. L. Dutra, N. B. da Costa, S. Alves and R. O. Freire, Lanthanide Contraction in Lanthanide Organic Frameworks: A Theoretical and Experimental Study, *J. Phys. Chem. A*, 2020, **124**, 7678.

45 R. B. Jordan, Lanthanide Contraction: What is Normal?, *Inorg. Chem.*, 2023, **62**, 3715.

46 S. Y. Zhang, X. Shu, Y. Zeng, Q. Y. Liu, Z. Y. Du, C. T. He, W. X. Zhang and X. M. Chen, Molecule-based nonlinear optical switch with highly tunable on-off temperature using a dual solid solution approach, *Nat. Commun.*, 2020, **11**, 2752.

47 H. Xiao, L. W. Ding, J. Y. Liu, Z. H. Jia, L. M. Cao, Z. Y. Du and C. T. He, Solid-state molecular dynamics of a torsion-variable ammonium embedded in a deformable supramolecular framework, *Chin. J. Struct. Chem.*, 2023, **42**, 100003.

48 H. Xiao, W. Y. Hu, Q. Wang, C. H. Zeng, H. H. Li, H. M. Liu, Z. Y. Du and C. T. He, Molecular rotators anchored on a rod-like anionic coordination polymer adhered by charge-assisted hydrogen bonds, *Phys. Chem. Chem. Phys.*, 2024, **26**, 3974.

49 S. Havriliak and S. Negami, A complex plane representation of dielectric and mechanical relaxation processes in some polymer, *Polymer*, 1976, **8**, 161.

50 K. Aizu, Possible Species of "Ferroelastic" Crystals and of Simultaneously Ferroelectric and Ferroelastic Crystals, *J. Phys. Soc. Jpn.*, 1969, **27**, 387.

51 *CrysAlisPro*, Rigaku Oxford Diffraction, The Woodlands, TX, 2015.

52 G. M. Sheldrick, *SHELX 96 Program for Crystal Structure Determination*, 1996.

